Mass transfer and shear rate on a wall normal to an impinging circular jet

Magdalena Kristiawan[1], Kodjovi Sodjavi[2], Brice Montagné[2], Amina Meslem*[3], Vaclav Sobolik[2]

[1] Unité Biopolymères Interactions et Assemblages, INRA, BP 71627, Nantes, France

[2] LaSIE, University of La Rochelle, Pôle Sciences et Technologie, avenue Michel Crépeau, 17042, La Rochelle, France

*[3] LGCGM EA3913, Equipe Matériaux et Thermo-Rhéologie, Université Rennes 1, IUT de Rennes, 3 rue du Clos Courtel, BP 90422, 35704 Rennes Cedex 7, France
amina.meslem@univ-rennes1.fr, Corresponding author

Abstract

The electrodiffusion technique and the time-resolved tomographic PIV were used in impinging jet issued from a convergent conical nozzle at a Reynolds number of 2450 based on the nozzle diameter *d* and the jet exit velocity. The relative distance from the nozzle to the impinging wall was equal to *h*/*d*=2. The experimentally gained velocity fields provides information on the organization of coherent flow structures, which play a role in the wall shear rate and the mass transfer phenomenon at the impinged wall.

Instantaneous wall shear rate and local mass transfer were measured at an impinging wall using platinum electrodes with a diameter of 0.5 mm flush mounted into a platinum disc electrode with a diameter of 49.5 mm. The small electrodes were used alternately for the measurement of wall shear rate and mass transfer. The proposed correction factor on the inertia of the concentration boundary layer, which is the ratio of the corrected fluctuations of wall shear rate to their primary values, along with the analysis of the signals history, provide valuable information on the state of the hydrodynamic boundary layer. The mean wall shear rate and local mass transfer exhibit their maximum values at the normalised radial positions *r*/*d* = 0.6 – 0.7. There are the interactions of the primary Kelvin-Helmholtz (K-H) vortices with smaller structures issued from the breaking-down of these vortices, both rotating in the same direction. Counter-rotating secondary vortices form between the wall and primary K–H vortices at a radial distance about *r*/*d* = 1.5. They are present in a wide region (*r*/*d* ~ 1.5 to 2.5); around *r*/*d* = 1.5 they are very close to the wall leading to a clear periodicity of wall shear rate, and at *r*/*d* = 2.5 they are farther above the wall since no periodicity of the wall shear rate was observed. The

local mass transfer rates were integrated and compared with the global mass transfer measured by a platinum disc electrode.

Keywords—Electrodiffusion, Time-resolved tomographic PIV, impinging round jet, wall shear rate, mass transfer

List of symbols

c	bulk concentration of active ions, mol/m^3
D	diffusion coefficient of active ions, m^2/s
d_{disc}	platinum disc diameter, m
F	Faraday constant, 96 485 C/mol
$f\#$	lens aperture
f	vortex shedding frequency, Hz
h	nozzle-to-plate axial distance, m
I	limiting diffusion current, A
i	instantaneous value
j	flux of active ions, mol/s
k	coefficient of mass transfer, $k = I/S_{el}nFc$, m/s
L	effective probe length, m
Nu	Nusselt number
n	number of electrons involved in the electrochemical reaction
N	number of samples
Pr	Prandtl number, $Pr = \nu / \alpha$
R	electrode radius, m
r	radial distance measured from stagnation point, m
Re	Reynolds number, $Re = U_{exit}d\rho/\mu$
Sc	Schmidt number, $Sc = \nu/D$
S_{el}	active surface of the electrode, m^2
Sh	Sherwood number, $Sh = kd/D$
St_θ	Strouhal number, $St_\theta = f\theta/U_{exit}$
(x, y, z)	system of coordinates attached to the nozzle, m
t	time, s
U_{exit}	jet exit mean velocity, m/s
U	velocity in x direction (streamwise velocity), m/s
V	velocity in y direction (normal velocity), m/s
W	velocity in z direction (spanwise velocity), m/s
α	thermal diffusivity, m^2/s
γ	wall shear rate, s^{-1}
γ_{cor}	corrected wall shear rate, s^{-1}
λ	thermal conductivity, W/mK
λ_2	vortex detection criterion, s^{-2}
ρ	density, kg/m
μ	dynamic viscosity, Pa s
ν	kinematic viscosity, m^2/s
ω_θ	azimuthal vorticity component, s^{-1}
ω_r	radial vorticity component, s^{-1}
θ	shear layer momentum thickness

Subscripts

G	global (space average) value
s	stagnation point

Superscripts

’	fluctuation value
–	time-averaged value

1. Introduction

The impinging jets are used in the applications requiring high heat and/or mass transfer rates. Numerous papers were published on the Nusselt number (*Nu*) distributions generated by impinging jets [1, 2], but only a few studies have been dedicated to the analysis of the corresponding wall shear rate (γ) distributions [3-6].

Mass transfer and wall shear rate were deduced from the velocity field close to the impinging wall, and such a field is usually subjected to great uncertainties [6]. To a few exceptions belongs the study of Kataoka et al. [4] who measured local mass transfer and wall shear rate using the electrodiffusion (polarographic) method and pressure fluctuations using a piezoelectric transducer. However they used different electrodes for mass transfer (circular electrodes) and for wall shear rate (rectangular electrodes) measurements. Hence these two phenomena were not measured at the same place. Based on the same experimental apparatus and electrodiffusion method, Kataoka and Mizushina [3] investigated the effect of the free-stream turbulence on the wall shear rate and the mass transfer in an impinging round jet at large Prandtl number ($Pr > 10^3$). The jet Reynolds number varied within a range [2800 - 32600] and a nozzle-to-wall distances h/d was equal to 3.9, 5.9 and 8.2, where d is the nozzle diameter which was a convergent conical type. The Nusselt number was deduced using an analogy between heat and mass transfer. The hot-wire anemometry technique was used for the free-stream velocity measurements in the neighbourhood of the target wall. The authors observed that the wall shear rate is almost unaffected by the free-stream turbulence, whereas the rate of mass transfer is greatly enhanced. The local enhancement of the mass transfer was attributed to the penetration of non-uniform turbulence of free-stream across the laminar boundary layer and to the subsequent transition from laminar to turbulent boundary layer.

Chin and Agarwal [7] used electrodiffusion method for the local mass transfer measurement and classical pressure measurement using holes in the impinging wall. Using the electrodiffusion method, Alekseenko and Markovich [8] measured local wall shear stress of impinging round jet. Chin and Tsang [9] used the same method for mass transfer measurements

from an impinging jet to the stagnation region on a circular disk electrode. They found that there is a uniform accessibility to mass transfer (the thickness of concentration boundary layer and mass transfer rate have constant values) in a range of R/d (0.1; 1) for turbulent nozzle flow and R/d (0.1; 0.5) for laminar flow, where R is the electrode radius and d the nozzle diameter. Beyond this uniform accessibility region the mass transfer rate was found to be a decreasing function of the lateral coordinate.

Kristiawan et al. [10] and Meslem et al. [11] calculated mass transfer rate in the impingement region from the measured wall shear rate in the vicinity of the stagnation point under the assumption of uniform thickness of hydrodynamic and concentration boundary layer.

The literature reveals that for high Reynolds numbers and low nozzle-to-wall distances h/d, two peaks are present on the radial distributions of local Nusselt number or local Sherwood number (Sh), produced by circular impinging jets. The first peak corresponds to the maximum of heat/mass transfer rate and occurs approximately at the nozzle radius. In some investigations [3, 12-14], the location of the first peak is observed from $r = 0.5d$ *to* $r = 0.7d$ for $h < 4d$. This peak is attributed to the high turbulence intensity at the nozzle edge and to the direct impingement of large toroidal Kelvin-Helmholtz (K–H) vortices originated in the mixing region [3]. The secondary peak occurs at the radial distance from the stagnation point ranging from $1.2d$ to $2.5d$ [3, 12-15]. The origin of this secondary peak is widely discussed in the recent reviews of Carlomagno et al. [16] and Zuckerman and Lior [17]. It is now recognized that this results from the unsteady separation of the counter-rotating secondary vortices which form near the wall bellow primary K–H vortices [16-19]. Some decades ago, when diagnostic techniques of the flow dynamics were still limited, the secondary peak was attributed to the transition from laminar to turbulent boundary layer in the wall jet region [3, 20].

With increasing Reynolds number, the location of the secondary peak moves outwards from the stagnation point and their imprint on heat/mass transfer increases [12].

The present paper is devoted to the characteristics of instantaneous wall shear rate and local mass transfer in an impinging round jet issuing from a convergent conical nozzle at a Reynolds number of 2450 and a nozzle-to-wall distance h/d=2. The experiments are performed using the electrodiffusion method [10, 11, 21]. For the first time, the wall shear rate and local mass transfer are measured at the same place. The fluctuations of the local Sherwood number have never been studied before.

2. Theory

2.1 Electrodiffusion method

The electrodiffusion method (ED) is based on the measurement of the limiting diffusion current (I) on a working electrode (probe). This current is due to the reaction of ions (active species) which are transported by convection and molecular diffusion to the working electrode. Mass transfer coefficient k can be deduced from the limiting diffusion current I

$$k = \frac{j}{S_{el}\, c} = \frac{I}{S_{el}\, n F\, c} \quad , \tag{1}$$

where j is the flux of the active ions, S_{el} is the active surface of the electrode, c is the bulk concentration of the active ions, n is the number of electrons involved in the electrochemical reaction and F is the Faraday constant.

The mass transfer coefficient calculated from Eq. 1 is the mean value over the electrode surface. The electrode can be arbitrary large but the k gives a surface averaged value. For measurements of local k it is necessary to embedded small electrodes in a large one. The limited diffusion current can be also interpreted as wall shear rate (γ). To fulfil necessary conditions, the electrode for γmeasurements must be sufficiently small and flush mounted in an inert wall or counter-electrode.

The redox reaction of potassium ferri- and ferrocyanide is frequently used in ED measurements. There is a reduction on the working electrode

$$Fe^{3+}(CN)_6^{6-} + e^- \rightarrow Fe^{2+}(CN)_6^{6-} \tag{2}$$

and oxidation on the auxiliary electrode. In order that the diffusion current is controlled only by the phenomena on the working electrode, the auxiliary electrode must be much larger than the working electrode. The effect of the auxiliary electrode can be also attenuated using higher concentration of ferrocyanide than ferricyanide. To eliminate the transport of ions by migration in electric field, the electric conduction is enhanced by addition of a supporting electrolyte which does not react on the electrodes.

2.2 Wall shear rate

Viscosimetric steady flow with parallel streamlines and uniform wall shear rate is the condition for the interpretation of limiting diffusion current as wall shear rate. The formula corresponding to Leveque's equivalent formula for heat transfer, established by Reiss and

Hanratty [22] is valid for the case when the molecular diffusion parallel with the surface can be neglected

$$\gamma = 0.0999\,(nFc)^{-3} D^{-2} R^{-5} I^{3} \qquad (3)$$

where D is the diffusivity of the active ions, and R is the radius of the electrode.

In the case of an impinging circular jet, the streamlines in the wall vicinity close to the stagnation point spread radially from this point. In this region, the wall shear rate increases linearly with the distance from the stagnation point. There is the effect of the velocity component normal to the wall on the probe reading which attenuates with increasing r. The limiting diffusion current at the stagnation point is a function of $\frac{d\gamma(r)}{dr}$. This current is finite even if $\gamma(r=0) = 0$. The error of using Eq.3 close to the stagnation point was treated by Kristiawan et al. [10]. This error decreases with r and it makes 2.1 % at a dimensionless radial distance r/R equal to 4.

Eq.3 was derived under the assumption that the velocity is a linear function of the distance from the wall with the slope equal to the wall shear rate. The Schmidt number in aqueous electrolyte is about 1410 and the concentration boundary layer is generally much thinner than the hydrodynamic boundary layer, hence, the hypotheses of linear velocity profile is fulfilled. However in unsteady flows the concentration boundary layer needs some time to develop. The inertia of diffusion boundary layer on the working electrode manifests itself as a filter which diminishes amplitude and causes a phase shift of the measured current. Menedez and Ramaprian [23] solved the heat transfer to a flush mounted sensor under periodical variation of the velocity parallel with the wall. Due to the thickness of the thermal boundary layer, they took into account the normal velocity component in the hydrodynamic boundary layer. Their solution contains three shape parameters which are function of time and depend on flow geometry. Sobolik et al. [24] supposed a viscometric flow with time dependent variation of uniform wall shear rate. Using integral mass balance of the mass transfer equation, they arrived to the relation between the wall shear rate and instantaneous limiting diffusion current:

$$\gamma_{cor} = \gamma\left[1 + 0.45 D^{-1/3} R^{2/3} \gamma^{-5/3} \frac{d\gamma}{dt}\right] \qquad (4)$$

where γ_{cor} is the corrected wall shear rate and γ the primary wall shear rate. The primary wall shear rate is calculated using the instantaneous measured limiting diffusion current using Eq.3 or similar equation obtained by the probe calibration. This correction contains only parameters which can be evaluated by the probe calibrations [24]. The expression in the brackets of Eq. 4

is the correction factor. The higher wall shear rate the lower is this factor. Eqs 3 and 4 were obtained under the assumption that the flow direction does not change. However there is unsteady azimuthal component in the wall jet region [18] which causes changes in the flow direction. This will result in some small error which cannot be estimated as this problem has not been solved until now.

2.3 Mass transfer

The mass transfer coefficient calculated from Eq. 1 is the mean value over the electrode surface. The electrode can be arbitrary large but the k gives a mean value. For measurements of local k it is necessary to embedded small electrodes in a large one. The same voltage is imposed on all working electrodes and the current through large electrode gives global coefficient while the currents through small electrodes give local coefficients of mass transfer. The Sherwood number is defined by:

$$Sh = \frac{k\,d}{D} \tag{5}$$

where d is the nozzle diameter and D the diffusion coefficient of active ions.

Although mass transfer is considered on the impinged solid wall, the chosen scaling length of the Sherwood number is the nozzle diameter d (Eq. 5). The jet core region, where the characteristics of the jet are nozzle-geometry dependent, still exists in the nozzle-to-wall distance $h/d = 2$, which is our case. Hence, the transfer phenomena occurring on the target wall at $h/d = 2$ are nozzle-geometry dependent and the relevant length scale is the nozzle diameter d.

3. Experimental setup

3.1 Wall shear rate and mass transfer measurements

Detailed description of the experimental device can be found in the papers by Kristiawan et al. [10], El Hassan et al. [21] or Meslem et al. [11]. It consists of a Plexiglass reservoir, a gear pump, a nozzle and a target with electrodes (Fig. 1a). The nozzle has a convergent conical form (Fig. 1b) with an exit diameter d of 7.8 mm and an area contraction 4:1 on a length of 17 mm. The nozzle is screwed to a 200 mm length stainless steel tube with the inner and outer diameters of 15 and 20 mm, respectively. A honeycomb, manufactured of 7 mm thick disc by

drilling 17 holes with a diameter of 2 mm, was fitted in the tube inlet. The temperature of the fluid was controlled by a cooling coil within ±0.2 °C.

The target, see Fig.1c, was manufactured of a Plexiglas disc with a diameter of 100 mm and thickness 17 mm by first drilling the holes to insert the electrodes. Platinum foil with a diameter d_{disc} of 50 mm and thickness 50 µm (designated in the following as platinum disc) was assembled centrally with Plexiglas disc using Neoprene glue. Holes with a diameter 0.7 mm were drilled through the platinum disc as a continuation of the holes in the Plexiglas disc. The electrodes were fabricated of a 0.5 mm platinum wire which was coated electrophoretically with a deposit of a polymeric paint. After soldering connecting cables, the electrodes were glued with an epoxy resin into the Plexiglas disc, so that the tops of the platinum wires just projected above the platinum disc. The wires were then rubbed down flush with the surface of the platinum disc using progressively finer grades of emery paper. The last emery paper had a grit size 10 µm. The whole surface was then polished using a fine dental paste. Before each series of test, the electrode surfaces were polished and rinsed with distilled water. Nickel sheets with an area of 0.15 m^2 and the stainless steel tube were used as the auxiliary electrode (anode). The area of the nickel sheets and the stainless steel tube was 80 times superior to the platinum disc area. To measure only the phenomena which happen on the measuring electrode (cathode), the area of the auxiliary electrode (anode) should be large enough. Measured currents in our experiments did not change if the anode area was enlarged which was the proof of the sufficiency of anode area.

The nozzle assembly was located on a support which allowed vertical movement for accurate alignment of the nozzle axis with the electrodes. The reservoir with the fixed target was placed on a sliding compound table which permitted horizontal displacement of the target relative to the nozzle. The wall shear rate and local mass transfer were measured at 18 positions separated by 1 mm. The first position of the stagnation point (see Fig. 1c) was in the point A (6.2 mm left from the disc centre), and the last position in the point B (10.8 mm right from the disc centre).

The test fluid was an aqueous solution of 5 mol/m^3 potassium ferricyanide ($K_3(Fe(CN)_6)$), 25 mol/m^3 potassium ferrocyanide ($K_4(Fe(CN)_6)$) and 1.5% mass potassium sulphate (K_2SO_4) as supporting electrolyte. The solution had a density of 1006 kg/m^3, kinematic viscosity $1.06 \cdot 10^{-6}$ m^2/s and diffusivity $7.5 \cdot 10^{-10}$ m^2/s at 20°C. The resulting Schmidt number was 1410.

The Reynolds number (Eq. 6) which is based on the nozzle diameter d and the mean exit velocity from the nozzle (U_{exit}= 0.33 m/s) had a value of 2450.

$$Re = \frac{U_{exit}\, d\, \rho}{\mu} \qquad (6)$$

The distance between the target and the nozzle exit plan h/d was equal to 2. The main parameters of the experiments are summarized in Table 1.

The voltage on the working electrodes was adjusted on -0.8 V; 5000 data were recorded at a frequency of 500 Hz at a radial position during 10 s for wall shear rate measurement, then the voltage was imposed also on the platinum disc and the same amount of data were recorded at the same frequency for the mass transfer study.

The electrodes were calibrated before and after every series of measurements using a voltage step transient [25]. The result of this calibration, i.e. the Cottrell coefficient which is proportional to ($c\, S_{el}\, D^{1/2}$), varied about ±4%. The estimated errors were ±8% and ±4% for the wall shear rate and the Sherwood number, respectively.

Table 1: The main parameters of the experiments

d (mm)	h (mm)	U_{exit} (m/s)	θ (mm)	f (Hz)	v (m²/s)	D (m2/s)	Re	St_θ	Sc
7.8	15.6	0.33	0.17	26	$1.06 \cdot 10^{-6}$	$7.5 \cdot 10^{-10}$	2450	0.013	1410

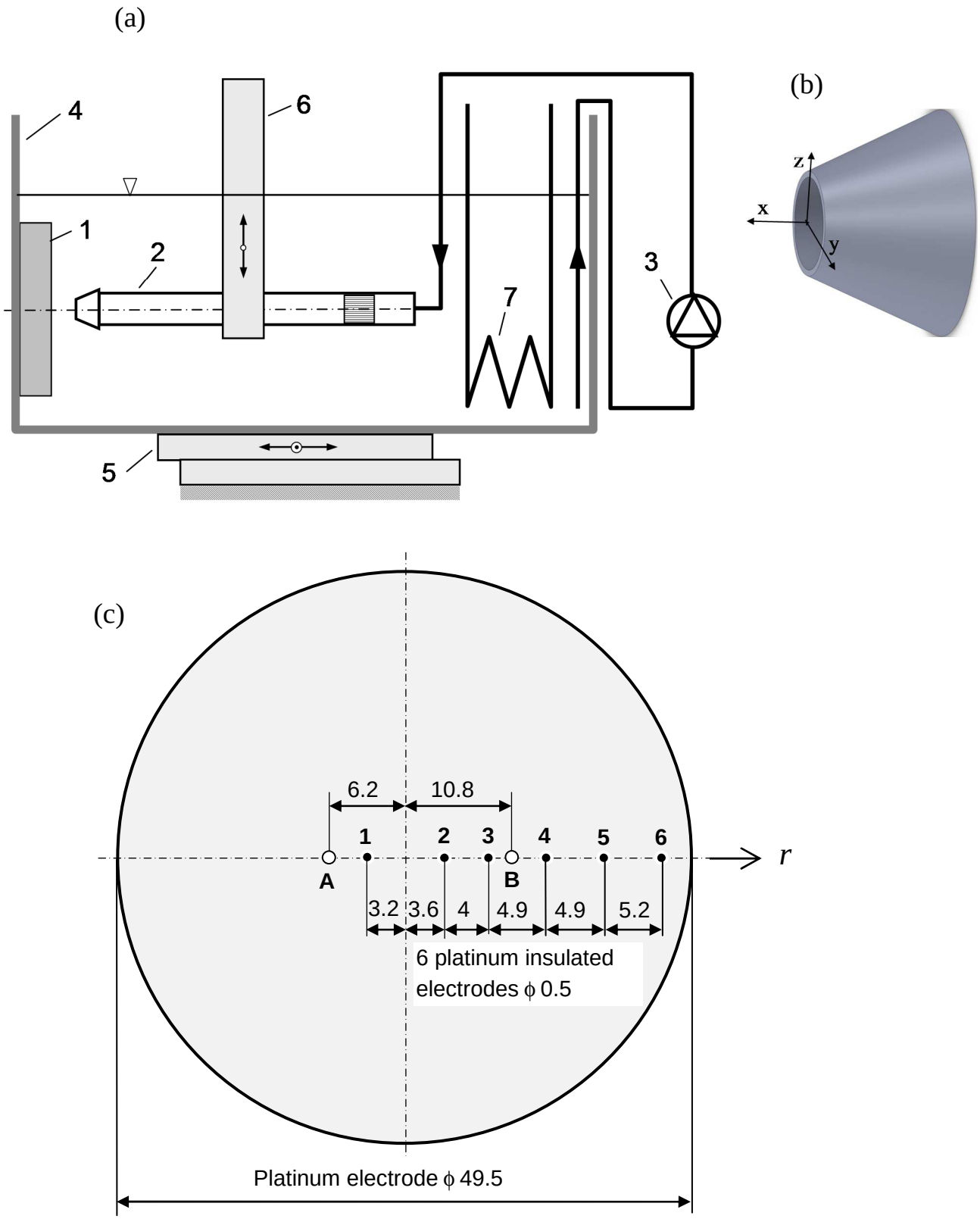

Fig. 1. (a) Diagram of apparatus: 1 target disc with electrodes, 2 tube with nozzle and honeycomb, 3 pump, 4 reservoir, 5 compound table, 6 nozzle holder, 7 cooling coil; (b) The system coordinates associated to the nozzle; (c) Platinum disc with six electrodes. A, B extreme positions of stagnation point displacement

3.2 Flow field measurements

The three-dimensional behavior of flow transition was investigated by the time-resolved tomographic particle image velocimetry. The emphasis was done on the organization of coherent flow structures, which affect the wall shear rate and mass transfer phenomenon at the impinged wall.

The PIV system consisted of high-repetition rate laser and three high-speed CMOS cameras (phantom V09, 1600×1200 pixel², 12 bit) equipped with Nikon objectives of 105mm focal length. The sketch of the experimental setup is shown in Fig. 2.

Two cameras were arranged in backscatter orientation with an angle approximately 20° relative to the normal of the viewing face of the light volume. The third camera was oriented normal to the viewing face of the light volume. The scheimpflug adapters were used to align the mid-plane of the illuminated area with the focal plane and the lens apertures were fixed to $f^{\#}=16$. The test fluid was seeded with titandioxide polyamide particles of 20 μm mean diameter. The illumination was provided by a pulsed, dual-cavity Nd:YLF laser with a power of 2×10mJ. A beam expander (volume optics of LaVision), composed of two cylindrical lenses and a rectangular slit, was used to generate a rectangular light volume. A mirror was inserted at the bottom of the reservoir to reflect the laser beam back to the measurement volume. The effective measurement volume was $2d\times6d\times5d$ with an average resolution of 29.75 pixels/mm. The particle image density was approximatively 0.04 particles/pixel. The imaging system was calibrated by the two-level spatial target (Type 7 target in the LaVision Software). In each of the two calibration planes, a third order polynomial fit was used to determine the transformation matrix which match the viewing planes of the three cameras with an accuracy of approximately 0.15 pixels.

In order to increase the illumination energy, 1000 images were recorded at a frequency of 1000 Hz in single frame mode with laser time interval $\delta t = 0\mu s$. The maximum particle displacement is 14 pixels. The images were reorganized in double frames reducing the measurement frequency to 500 Hz.

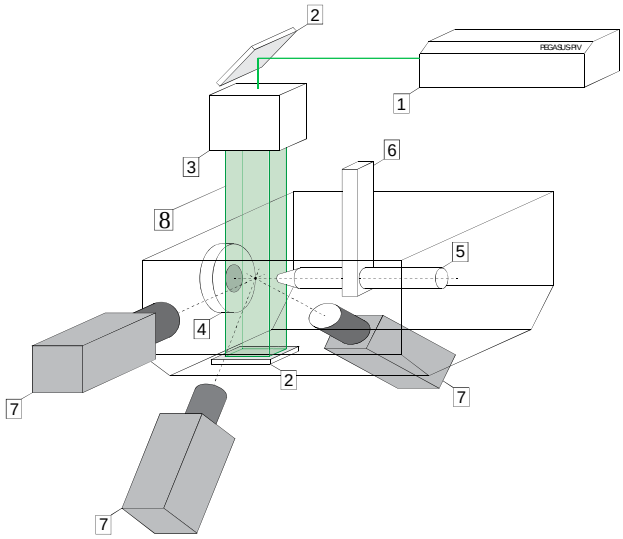

Fig. 2 Schematic of the experimental setup of tomographic PIV: 1 laser head, 2 mirror, 3 beam expander with rectangular slit, 4 target disc, 5 tube with nozzle, 6 nozzle holder, 7 phantom V09 cameras, 8 laser beam

Prior to the particle volume reconstruction, the original images were preprocessed to improve the reconstruction process. The main images preprocessing steps were described by Hain et al. [26]. A sliding minimum was subtracted from the images to reduce the background noise. A constant background due to laser reflecting or dirty Plexiglas was removed through an algorithmic mask, thus increasing the number of zero voxels. The particle image intensities were normalized by local image intensity, leading to similar particle intensity magnitude for the three cameras. Gaussian smoothing by 3×3 kernel was also applied. A geometric mask was used to define the boundaries of the calculated region.

The 3D particle positions within the volume were reconstructed using seven iterations of the Multiplicative Algebraic Reconstruction Technique (MART) algorithm provided by the LaVision software Davis 8.2.1. The volume was discretized with 520×1544×1188 voxels and a pixel to voxel ratio of 1. The volume self-calibration [27] showed an initial particle based calibration error of up to 2-3 pixels. After self-calibration correction the errors are reduced to below 0.15 pixels. At the present particle image density and number of cameras, the reconstruction quality Q is recognized to be above 0.75 [28, 29]. In this condition, the reconstruction should be assumed to be sufficiently accurate [29].

The vector fields were obtained by performing multi-pass direct cross-correlation using a final interrogation volume of 64×64×64 voxels ($0.28d$×$0.28d$×$0.28d$) and 75% overlap between adjacent interrogation boxes. The resulting vector spacing in each 3D velocity distribution is

0.07*d*. The spatio-temporal noisy fluctuations were reduced by using a second order polynomial filter over a kernel size of 5 grid nodes in space and 5 steps in time [13]. The spatial resolution of the filtered data remained equal to 0.28*d* whereas the temporal resolution was reduced to 8ms. The corresponding frequency of 125 Hz was approximatively five times greater than the vortex shedding frequency (26 Hz) of the studied jet flow.

The local mass conservation principle was used in numerous studies [13, 30, 31] to estimate the random velocity error in tomographic PIV measurements. In fact, when the flow is incompressible, the divergence of the 3D velocity fields should be zero. However, this is not the case when there are measurement errors and numerical truncation in the spatial discretization. When a second order central difference scheme is used to calculate the velocity gradients, assuming uniform vector spacing Δ, and uniform random error in all directions, the velocity gradient error is given by:

$$\delta\left(\frac{\partial u_i^{'}}{\partial x_i}\right) = \sqrt{\frac{3}{2\Delta^2}}\,\delta(u) \qquad (7)$$

where $\delta\left(\frac{\partial u_i^{'}}{\partial x_i}\right)$ is the RMS fluctuation divergence and $\delta(u)$ the random error.

In this study the mean random error was found to be around 0.48 pixel, corresponding approximatively to 4.4% of the streamwise velocity in the free jet region. Note that a random error varying between 0.60 and 0.42 pixel were reported by Atkinson et al. [30] and Buchner et al. [31] in turbulent boundary layer.

4. Results and discussion

4.1 Initial conditions

Fig.3 compares mean velocity profiles (Fig. 3 a) and RMS velocity (Fig. 3 b) close to the nozzle exit (x/d = 0.1), measured using the 2D PIV [21] and the 3D tomographic PIV.

While rather good agreement between mean velocity profiles was observed in the jet core region, discrepancies appeared in the shear layer region. Discrepancies were also observed in the RMS velocity profiles (Fig. 3 b).

The observed discrepancies could be attributed to the difference of the spatial resolution between the two measurement technics. Indeed, the 2D PIV measurements [21] were obtained with a spatial resolution of 0.13*d*×0.13*d*×0.13*d* (the third direction corresponds to the 1mm thickness of the laser) while the spatial resolution of the 3D PIV was 0.28*d*×0.28*d*×0.28*d*, which is ten times greater than that in 2D PIV measurements.

Anyway, comparisons are satisfactory which gives confidence in the tomographic PIV used in the present study.

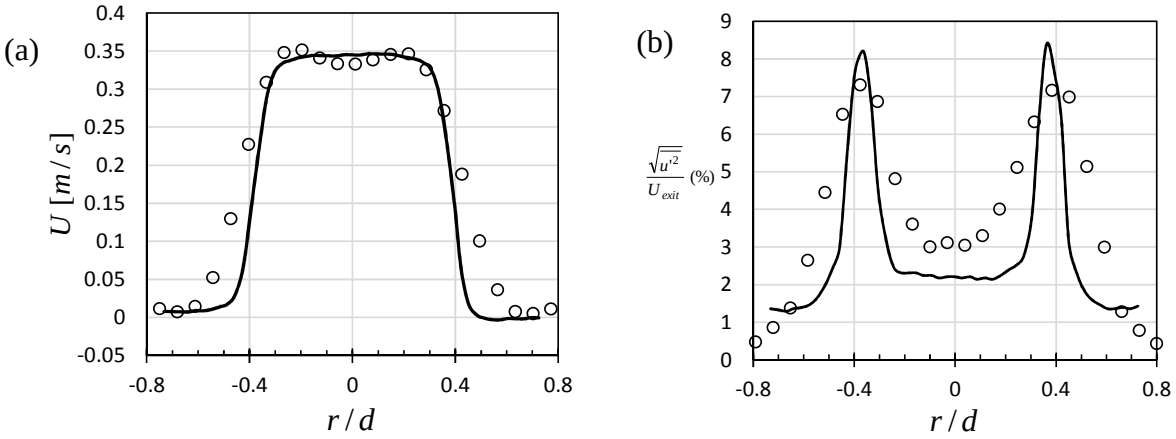

Fig. 3 Mean streamwise velocity (a) and normalised longitudinal root-mean-square (b) distributions at 0.1*d* from the exit - 2D PIV [21] (straight line), 3D tomographic PIV (circle)

4.2 Jet flow characteristics

As outlined previously, the tomographic PIV measurements were done with the objective to capture the organization of coherent flow structures, which play a role in the wall shear rate and the mass transfer phenomena at the impinged wall.

The three-dimensional flow organization of the jet is given in Fig. 4. This figure gives a temporal sequence of iso-surfaces of azimuthal vorticity $\omega_\theta d/U_{exit} = 3.3$, radial vorticity $\omega_r d/U_{exit} = \pm 1.1$and axial velocity $U/U_{exit} = 1.0$. The time interval between the displayed snapshots is $\Delta t U_{exit}/d$ = 0.63.

Vortex structures are often identified from experimental velocity fields using the vorticity. However, the vorticity is not always convenient for this purpose as it cannot distinguish between pure shearing motion and swirling motion. The most convenient method for vortex identification is the λ_2-criterion based on the local pressure minimum [32]. This method was applied to the velocity fields of the Fig. 4 and the results are given in Fig. 5.

The jet exhibited azimuthally coherent ring vortices which were shed between *x*/*d* = 1 and 1.5. These vortices resulted from the growth of Kelvin-Helmholtz (K-H) waves which rolled up into vortex rings that were carried downstream. The spectra (Fig. 6) of the streamwise velocity component *U* and transverse velocity component *V* in the free jet region at the position *x*/*d* =

1.2 and r/d = 0.6, exhibit a fundamental frequency of vortex shedding phenomenon equal to 26 Hz. This frequency leads to a Strouhal number based on the initial momentum thickness θ and the jet exit mean velocity U_{exit}, St_θ = 0.013 (see Table 1). This value is in a good agreement with values reported in the literature for free circular natural jets. For example, Gutmark and Ho [33] reported Strouhal number in the range 0.013 to 0.023 for the Reynolds number in the range 10^4 to 10^5.

In a free round jet [34], the K-H vortices become three-dimensional after one or multiple pairing, and eventually break down at the end of the jet potential core which extends to 5-6d [35]. In the present study, the target plate was placed at a distance h=2d, where the structures were still well organized and no pairing took place.

As shown in Fig. 5(b), the K-H vortices were very close to the wall in the wall jet region (r/d = 1.5) and beginning with r/d = 2 they draw far apart the wall.

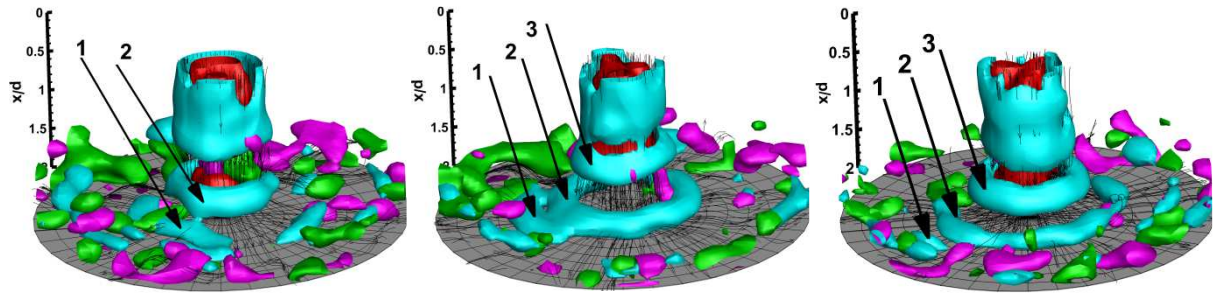

Fig. 4 Time sequence of stream traces and instantaneous iso-surfaces of azimuthal vorticity $\omega_\theta d/U_{exit} = 3.3$ (cyan), radial vorticity $\omega_r d/U_{exit} = -1.1$ (purple) and 1.1 (green) and axial velocity $U/U_{exit} = 1.0$ (red). The time interval between the displayed snapshots is $\Delta t U_{exit}/d$ = 0.63

In order to visualise the imprint of the K-H vortices on the target, the y-z presentation of the iso-lines $\lambda_2 d^2/U_{exit}^2 = -1.5$ at x/d =1.8 (i.e., at 1.6 mm from the target) is given in Fig. 7, along with iso-colors of axial velocity U/U_{exit} and projection of velocity vectors on the plane y-z. When the K-H vortices approached the wall, they stretched and their diameter increased, see Figs 4, 5 and 7. The same observation was done by Popiel and Trass [19] using the smoke-wire flow visualization technique. These authors have shown that at nozzle-to-plate separation h/d = 1.2, the toroidal vortices of the circular jet reached the plate at a radius r = 0.7d –0.9d, which is consistent with the present results (Fig. 7).

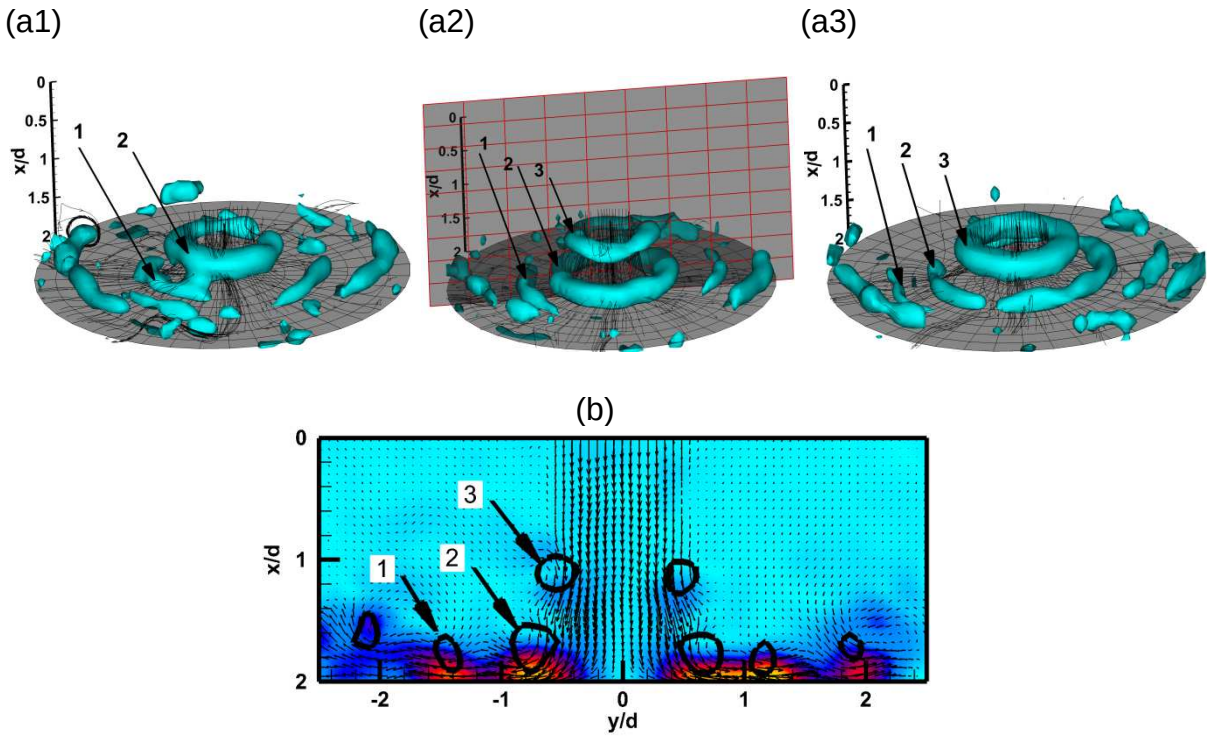

Fig. 5 (a) Time sequence of stream traces and instantaneous iso-surfaces of $\lambda_2 d^2 / U_{exit}^2 = -1.5$ (cyan). The viewing angle, the time instants and order are the same as in Fig. 4
(b) View in the vertical plane of the second instant (a2) –velocity field, iso-colors of the transverse velocity and iso-lines of $\lambda_2 d^2 / U_{exit}^2 = -1.5$

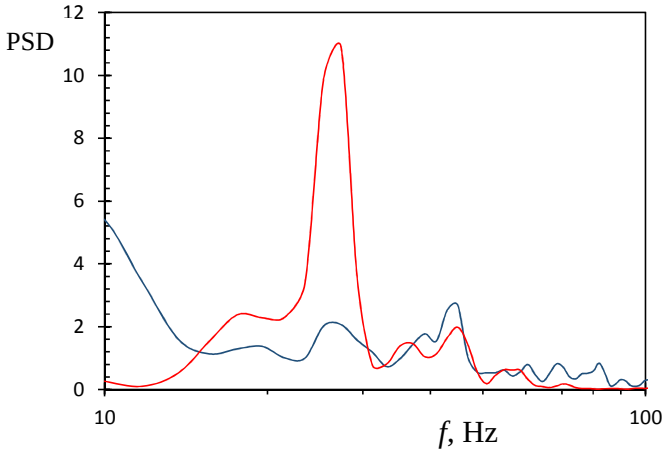

Fig. 6 Spectra of *U* (the dark line, blue online) and *V* (the light line, red online) normalized by their respective RMS values, at $r/d = 0.6$ and $x/d = 1.2$

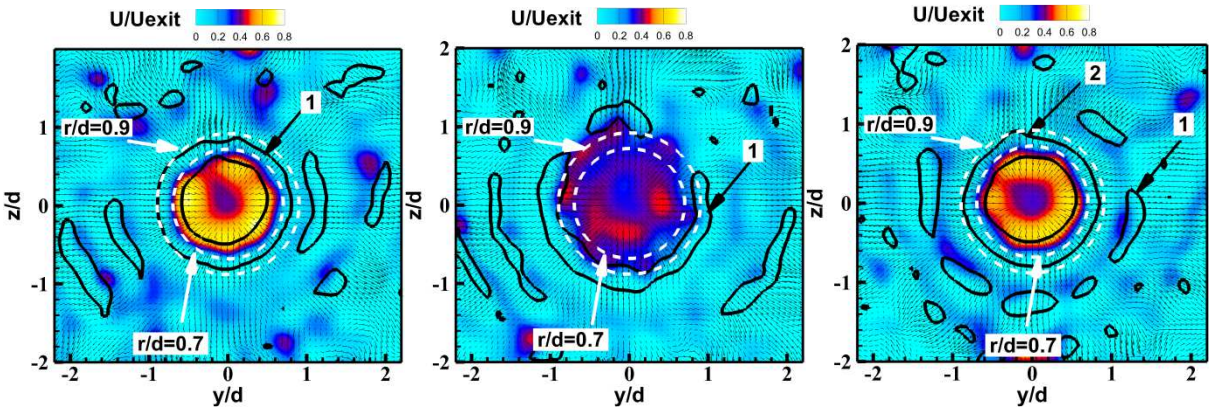

Fig. 7 Time sequence of instantaneous iso-colors of axial velocity U/U_{exit} with iso-lines of $\lambda_2 d^2/U_{exit}^2 = -1.5$ (black lines) and projection of velocity vector on y-z plane at axial location $x/d = 1.8$

4.3 Mass transfer and wall shear rate

The wall shear rate and mass transfer measurements were carried out alternately. The stagnation point was adjusted at a selected radial distance *r* (see Fig. 1) and wall shear rates γ were measured by the platinum wires working as cathode. Keeping the same position of the stagnation point, local mass transfer was measured by the platinum wires and global mass transfer by the platinum disc (both working as cathode). The nickel sheets were used in the both cases as anode.

The local time averaged Sherwood numbers ($\overline{Sh}$) measured with the six electrodes are shown in Fig.8 as a function of radial position *r*. Note that the radial distribution was constructed using 18 data series corresponding to 18 positions of the stagnation point between the points A and B of the platinum disc (Fig. 1). Hence, 6×18= 108 currents were used for the construction of such radial distribution of $\overline{Sh}$. The scatter of measured values is less than ±10% relative to the polynomial fit.

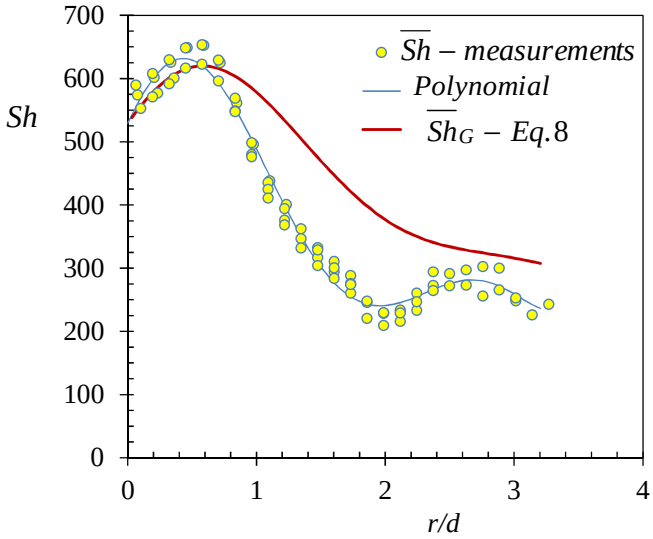

Fig. 8 Experimental values of local Sherwood number, polynomial 6 degree and calculated global Sherwood number

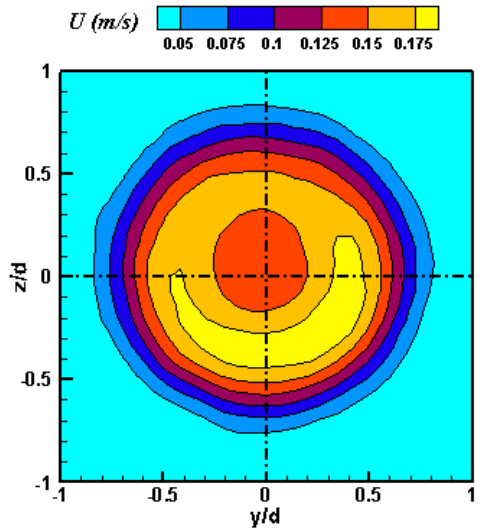

Fig. 9 Iso-contours of time-averaged axial velocity in the y-z plane at x/d=1.8

Fig. 10 (a) Time averaged local Sherwood number and wall shear rate as a function of normalised radial position r/d ; (b) Fluctuations of local Sherwood number and wall shear rate; (c) Relative fluctuations of local Sherwood number and wall shear rate; (d) Correction factor - Triangles stand for wall shear rate and circles for Sherwood number

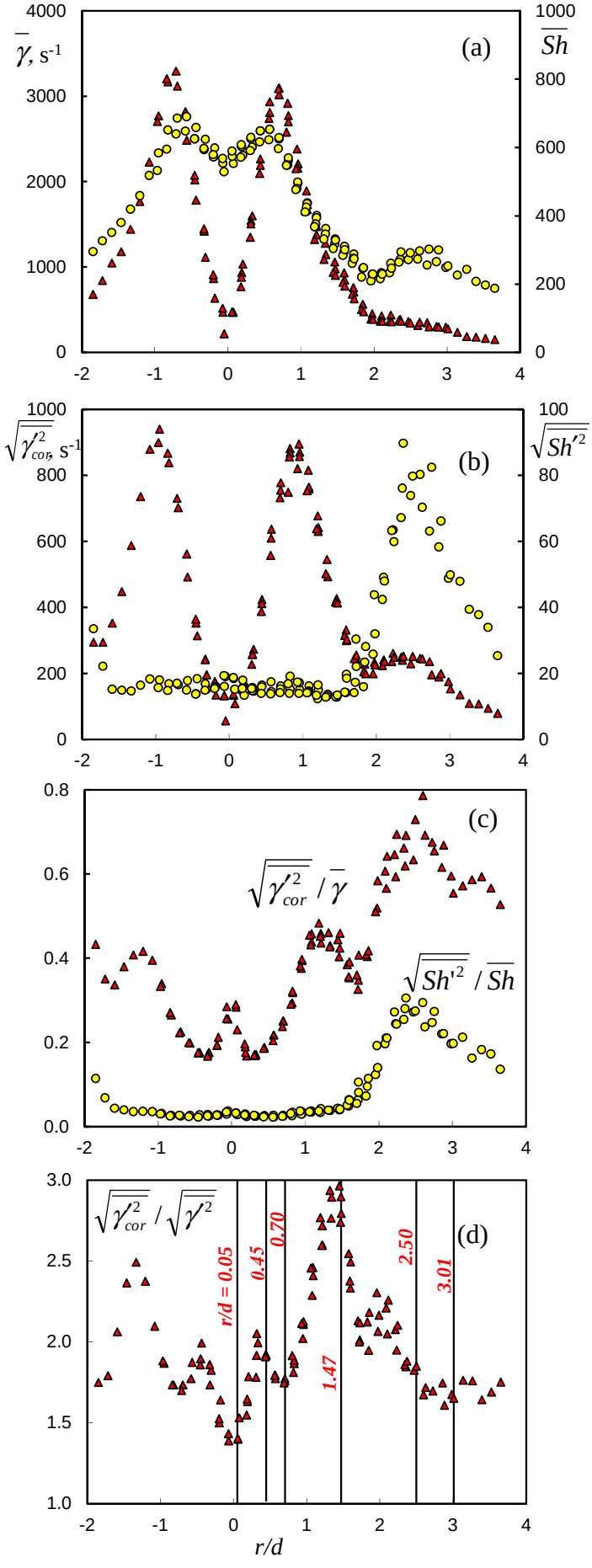

The local Sherwood number $\overline{Sh}$ slightly increases in the stagnation region ($0 < r < 5$ mm) and the maximum occurs at $r = 0.57d$, a distance little greater than the nozzle radius. The concentration boundary layer has not a constant thickness as was also observed by Kataoka et al. [4] in the jet core region of convergent impinging jet. Due to the increasing fluctuations of γ, the $\overline{Sh}$ increases. The mass transfer is very sensitive to the velocity turbulence which is still low on the jet axis in the potential core region and increases near the nozzle edge. Vallis et al. [36] observed a maximum of $\overline{Sh}$ at the stagnation point using nozzle to plate distance in the range 5 to 20 nozzle diameters. The jet core region is already consumed at 5*d*, a position from which the turbulence rises on the jet axis. In numerous studies of heat transfer (see for example Lee and Lee [12] or Colucci and Viskanta [37]) the same behavior was observed for the local time-averaged Nusselt number distribution: the maximum of $\overline{Nu}$ in the jet core region is shifted from the stagnation point when the jet core region exists, whereas in the jet transition region and downstream the maximum of $\overline{Nu}$ appears at the stagnation point. When *h*/*d* falls in the jet core region, the position of maximum of $\overline{Sh}$ or $\overline{Nu}$ depends on the transverse area of the core which decreases when *h*/*d* increases. The growth of the K-H vortices downstream from the jet exit is accompanied by the shrinking of the jet potential core. Thus, the K-H rings increase in diameter and occupies the space freed by the potential core and increase the turbulence in that space. This is the reason why the peak in $\overline{Sh}$ spreads towards the stagnation point when *h*/*d* increases. At the end of the jet core region, the turbulence reaches the jet axis and the peak of $\overline{Sh}$ moves into the stagnation point.

There is a secondary peak in $\overline{Sh}$ distribution (Fig. 8 and 10a). This secondary peak of $\overline{Sh}$ appears approximately at $r/d = 2.5$. This is consistent with the results of the literature which reports that the secondary peak in Nusselt or Sherwood number distribution occurs at the radial distance from the stagnation point ranging from 1.2*d* to 2.5*d* [3, 12-15]. Kataoka and Mizushina [3] observed the second peak at $r/d = 2.2$.

The time averaged local Sherwood number $\overline{Sh}$ was fitted by a polynomial of six degree. The global Sherwood number $\overline{Sh}_G$ was obtained by integration of $\overline{Sh}$ using this polynomial:

$$\overline{Sh}_G(r) = \frac{2}{r^2}\int_0^r \overline{Sh} \times \rho \, d\rho \qquad (8)$$

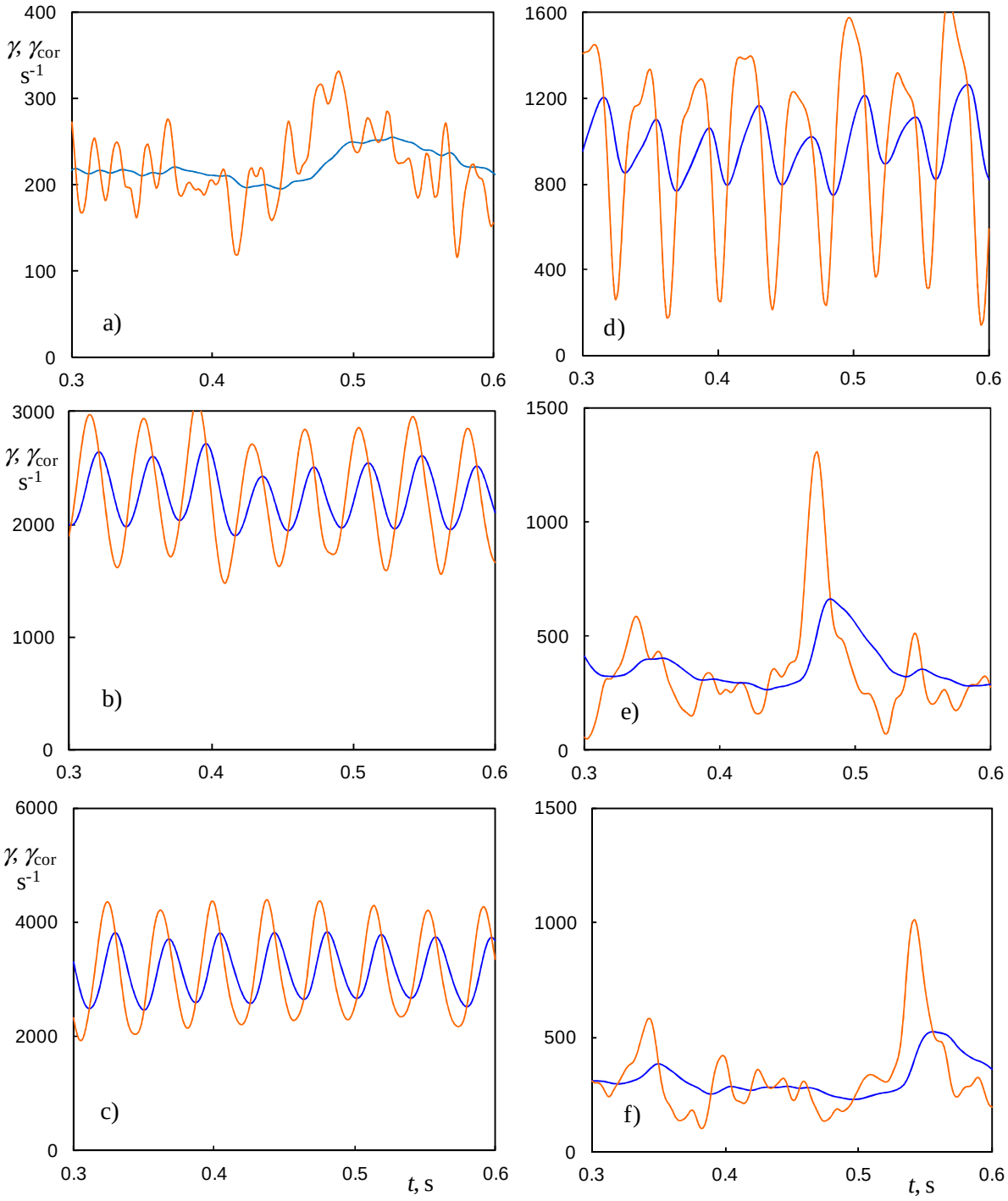

Fig 11. History of primary (the dark line, blue online) and corrected values (the light line, red online) of wall shear rate: a) *r/d* = 0.05; b) 0.45; c) 0.70; d) 1.47; e) 2.50; f) 3.01 – the radial positions are indicated in Fig. 10d

The global Sherwood number $\overline{Sh}_G$ at r = 24.75 mm was compared to the global Sherwood number obtained directly from the limiting diffusion current through the platinum disc (d_{disc}=49.5 mm) when the stagnation point was centred on the disc. The value $\overline{Sh}_G$ =305 obtained by integration of the $\overline{Sh}$ was about 8.5% higher than the value of 281 obtained by direct measurement technique. This difference can be due to the insulating annular gap around the electrodes where partial renewal of the active species can take place, especially when fluctuating velocity component normal to the wall is present. There can be also edge effects of electrodes which enhance the mass transfer [9]. Furthermore, Eq. 8 assumes an axial symmetry of the jet flow on the target, which is not perfectly true, particularly in the present study where the Reynolds number is low (see Fig. 9). Indeed, the low-Reynolds jet flows are sensitive to the slightest experimental disturbance or the slightest defect.

All the measured quantities are compared in Fig. 10. The time averaged values $\overline{\gamma}$ of wall shear rate and time averaged values $\overline{Sh}$ of Sherwood number are shown in Fig. 10a. The wall shear rate is theoretically zero at the stagnation point. This value cannot be measured because (i) there is still a current even if the γ is zero and (ii) the stagnation point can oscillate about the jet axis. The time averaged value $\overline{\gamma}$ of wall shear rate increases almost linearly in the stagnation region (see Fig. 10a). Using the procedure described by Kristiawan et al. [10] and Meslem et al. [11], the slope of a tangent to $\overline{\gamma}$ in the stagnation region which passes through 0 at r = 0 has a value of $6.35 \cdot 10^5$ $m^{-1}s^{-1}$ which corresponds to the Sherwood number at the stagnation point $\overline{Sh}_S$ of 573. This value compares quite well to the values of $\overline{Sh}$ in the stagnation region ($0<r<5$mm) which varies from 550 to 650 (Fig. 10a). Extrapolating the relation (Eq. 9) published by Chin and Tsang [9] for a nozzle with constant circular cross section (tube) and laminar flow $Re<2000$ to our conditions, the $\overline{Sh}_S$ equals to 820. Evidently the difference in $\overline{Sh}_S$ is due to the different flow conditions.

$$\overline{Sh_s} = 1.50\, Re^{1/2} Sc^{1/3} (H/d)^{-0.054} \qquad (9)$$

As shown in Fig. 10a, the maximum of wall shear rate $\overline{\gamma}$ is at r/d = 0.69. Alekseenko and Markovich [8] found the maximum of wall shear rate at r/d = 0.7 for a wide range of Re (6300; 55000), which is consistent with our results. Note that the maximum of $\overline{Sh}$ is closer to the stagnation point (r/d =0.57) than the maximum of $\overline{\gamma}$. According to Kataoka and Mizushina [3], the heat/mass transfer in the impinging region is much more sensitive to the amplified

turbulence at the free-stream than the wall shear rate. The vortex dynamics in the impinging region for *Re* = 2450 captured using PIV (Figs 4-7) can explain $\overline{Sh}$ and $\overline{\gamma}$ maxima and their respective positions. The K-H vortices, which develop in the jet shear layer (the centre of the K-H structure is around *r*/*d*= 0.5), approached the target wall normal to it, and are deflected radially in the region *r*/*d*= 0.5-0.7 before impinging the wall around *r*/*d* = 0.7 (Fig. 7). The peak in the wall shear rate $\overline{\gamma}$ corresponds to the region where the K-H vortices impinge the wall, whereas the maximum of $\overline{Sh}$ appears in the deflection region of the K-H vortices. As already suggested in [3], the turbulence in the free-stream, caused by the K-H when they are deflected at the vicinity of the wall, penetrate the laminar boundary layer and produce a local maxima in heat/mass transfer. That is why the maximum of $\overline{Sh}$ appears slightly closer to the stagnation point than the maximum of $\overline{\gamma}$.

The fluctuations of wall shear rate and Sherwood number are shown in Fig. 10b. They were calculated as standard deviation:

$$\sqrt{\overline{\gamma_{cor}'^2}} = \sqrt{\frac{\sum_{i=1}^{N}(\gamma_{icor} - \overline{\gamma_{cor}})^2}{N-1}}, \quad \sqrt{\overline{Sh'^2}} = \sqrt{\frac{\sum_{i=1}^{N}(Sh_i - \overline{Sh})^2}{N-1}} \qquad (10a, b)$$

where the index *i* stands for instantaneous value and *N* is the number of samples. The corrected values of γ were calculated using Eqs 3 and 4 and the Sherwood number using Eqs 1 and 5. It should be noted that the correction on the inertia of the concentration boundary layer affects the instantaneous values of γ and its standard deviation $\sqrt{\overline{\gamma'^2}}$, but the effect of the corrections on the values of $\overline{\gamma}$ are less than 2%. The fluctuations of wall shear rate increase with increasing distance from the stagnation point and achieve their maximum at *r*/*d* = 0.9, i.e. farther from the stagnation point than the maximum of $\overline{\gamma}$. The position of the maximum of the standard deviation of wall shear rate was found to be a function of *Re* [8], i.e. at *r*/*d* = 1 and 1.9 for *Re*= 6300 and 55000, respectively. Fluctuations of the Sherwood number $\sqrt{\overline{Sh'^2}}$ are low and almost constant until *r*/*d* =1.47 where they start to increase. The maximum of $\sqrt{\overline{Sh'^2}}$ and also local maximum of $\sqrt{\overline{\gamma'^2}}$ are placed at *r*/*d* =2.5 where a second peak of the mean Sherwood number was observed (Fig. 8 and Fig. 10a). The second local maximum in heat/mass transfer is related

to the appearance of the unsteady separation of the induced secondary vortices that form near the wall under primary K–H vortices [12-15, 38].

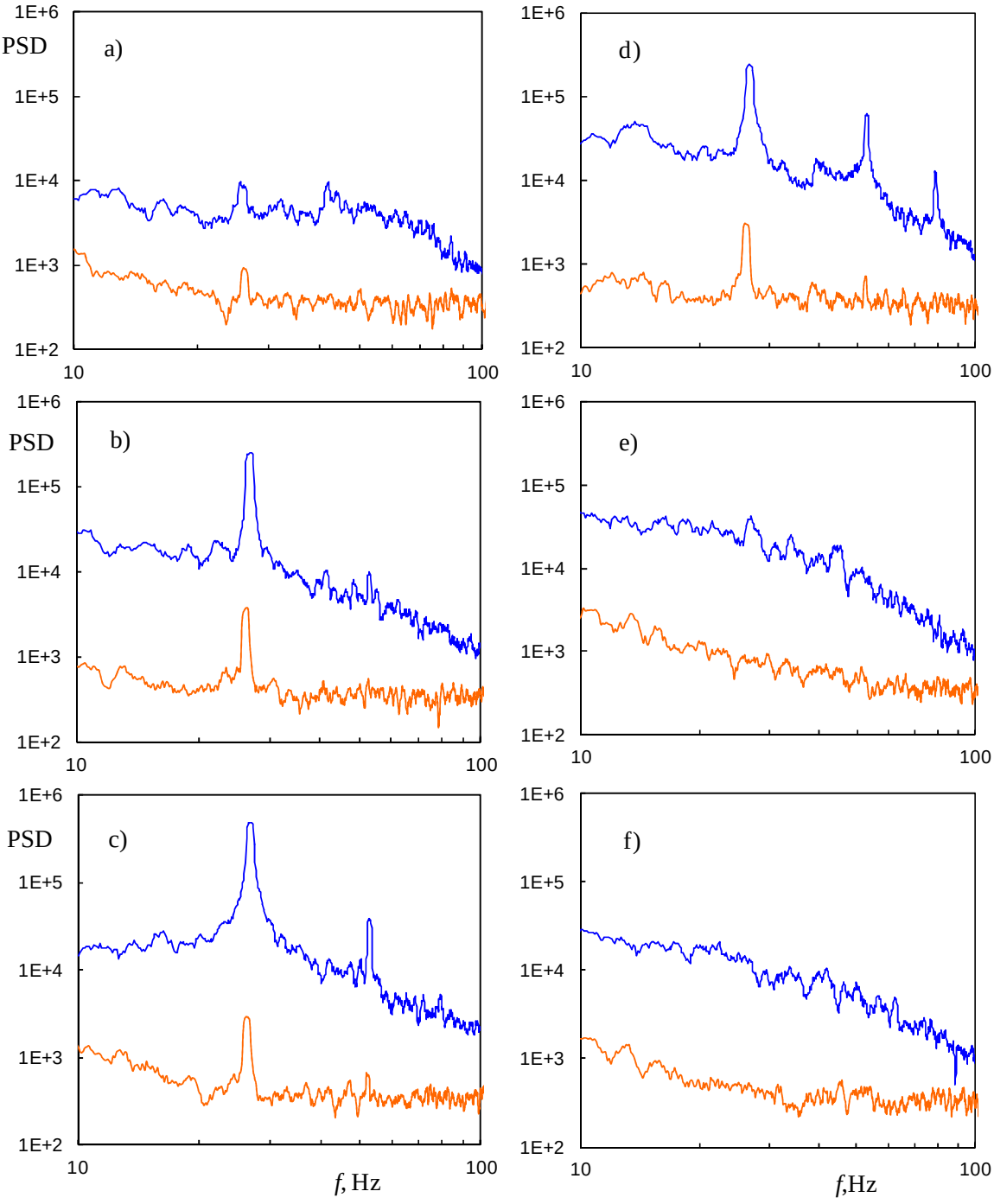

Fig. 12 Spectra of γ_{cor} (the dark line, blue online) and *Sh* number (the light line, orange online). The conditions correspond to Fig. 11: a) *r/d* = 0.05; b) 0.45; c) 0.70; d) 1.47; e) 2.50; f) 3.01– the radial positions are indicated in Fig. 10d

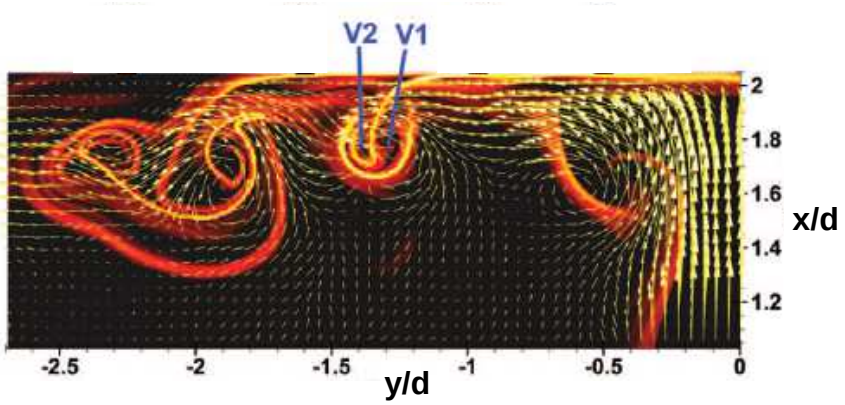

Fig. 13 The secondary vortex (V2) generated under the primary structure (V1) in a circular impinging jet (adapted from [38]).

The relative fluctuations of γ and *Sh*, i.e. the fluctuations divided by the corresponding mean values are shown in Fig. 10c. While the curve shape of the relative fluctuations of *Sh* does not differ much from that of $\sqrt{\overline{Sh'^2}}$, the relative fluctuations of γ exhibit another course. There is a local maximum at the stagnation point which can be attributed to the displacement of the stagnation point due to the jet flapping. The second local maximum is at r/d =1.2 where the time averaged values of γ and *Sh* (Fig. 10a) change their slope. The maximum of the both relative fluctuations is at r/d=2.5 (Fig. 10c).

The correction of the instantaneous value of γ on the inertia of the concentration boundary layer allowed us to define a new criterion. The ratio of the fluctuations calculated of the corrected values γ_{cor} (Eq. 4) to the fluctuations of the primary values is shown in Fig. 10d. We shall call the ratio $\sqrt{\overline{\gamma_{cor}'^2}} / \sqrt{\overline{\gamma'^2}}$ correction factor in the following. The maximum of correction factor is 3 at r/d=1.47. The effect of different flow regimes on the correction factor will be discussed later. The correction factor depends on the effective probe length (L) in the flow direction (L= 1.64**R* for a circular electrode of radius R [39]). The concentration boundary layer on small probes is thin and the probe reacts the faster the smaller is its length. Hence the small probes used by Alekseenko (L=0.03 mm) and Kataoka (L=0.2 mm) would give smaller values of the correction factor, but their dependence on radius will be similar.

The histories of corrected and primary wall shear rates are shown in Fig. 11 at different radial positions (the chosen radial positions are indicated in Fig. 10d), and the corresponding power spectral density calculated of corrected values are given in Fig.12. The corrected γ passes through the local minima and maxima of the primary γ. According to Eq. 4, the corrected value

is equal to a primary value if the derivative of primary value is zero. Close to the stagnation point r/d = 0.05 (Fig. 11a) the values of wall shear rate and its fluctuations are rather low. The fluctuations are due to the displacement of the stagnation point with a weak periodicity of 26.1 and 44.3 Hz (see Fig. 12a). At a radial position r/d=0.45 (Fig. 11b), which is near the region where the periodic K-H vortices strike the target (Fig. 7), the oscillations of the wall shear rate are sinusoidal with a single frequency of 26.1 Hz (see Fig. 12b). This frequency is equal to the vortex shedding frequency captured using tomographic PIV (Fig. 6). At r/d=0.45 the correction factor is about 2. It should be noted that the frequency 26.1 Hz is imposed by the gear pump which is very close to the own frequency of the jet. Indeed, as mentioned earlier, the obtained Strouhal number St_θ = 0.013, falls in the range [0.013-0.023], which characterize the shear layer mode of the circular natural free jet [33].

The history of wall shear rates close to the maximum of γ, at r/d=0.70, is shown in Fig. 11c. The course is regular and periodical but the increase of γ is more rapid than its decrease (the slope of increasing phase is steeper than in the decreasing one) which correspond to “sharp peaks” and “large valleys” of corrected (true) wall shear rate (see Fig. 11c). It is the reason why a second frequency of $2f$ = 52.2 Hz appeared in Fig.12c. This course of wall shear rate with a slower decrease than increase, and the presence of the first harmonic at this position can be explained by the interaction of the primary K-H structures with smaller structures issued from the breaking-down of the primary K-H structures (see Figs 4 and 5) which rotate in the same direction. At this position, the correction factor has a local minimum equal to 1.75. Due to high values of wall shear rate the inertia of the concentration boundary layer is minimal here.

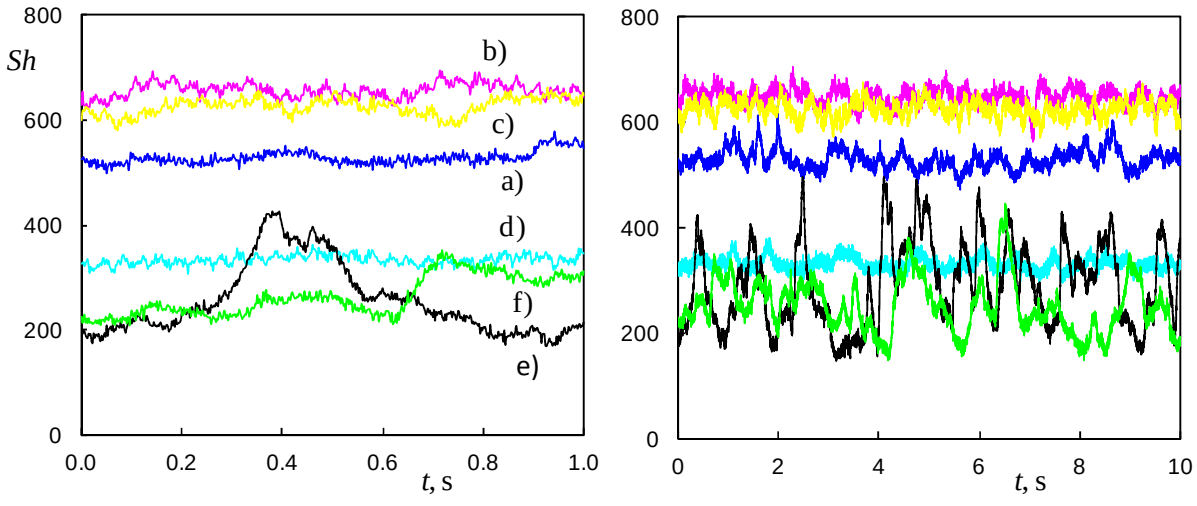

Fig. 14 History of Sherwood number in time scales 1 s (left) and 10 s (right): a) r/d = 0.05; b) 0.45; c) 0.70; d) 1.47; e) 2.50; f) 3.01– the radial positions are indicated in Fig. 10d

The wall shear rates at a maximum of correction factor (2.95), at r/d=1.47, are shown in Fig. 11d. The inertia of the concentration boundary layer has a high value at this position. The course of γ is periodic with a slower increase than decrease. The increasing phase shows irregularities which are amplified in γ_{cor}. The corrected wall shear rate has minima close to zero and it is distorted at maxima. In consequence, there are three peaks (26.1, 52.2 and 78.3 Hz) at the corresponding spectra (see Fig. 12d). During the impact on the wall, the rotating coherent structures create the wall shear rate with the same sign as the wall shear rate of the main stream. Passing of these structures along the probe manifests in maxima of wall shear rate. Secondary counter-rotating vortices are formed at the place where these vortices detach from the wall. These secondary vortices are at the origin of the secondary peak in heat/mass transfer distribution occurring at the radial distance ranging from 1.2d to 2.5d [12-15, 38].
It should be noted that the spatial resolution (0.28d×0.28d×0.28d) of the tomographic PIV technic used in the present study do not allow to capture this secondary structure, captured previously by the 2D PIV technic in [38] (see Fig. 13).

The values of γ_{cor} close to zero can be explained by these secondary vortices [18, 19]. The effects of the drifting velocity and rotation of secondary vortices are opposite and results in a wall shear rate close to zero [40]. From the behaviour of primary wall shear rates we can make conclusion that there is no reversing flow. Reversing flow would manifest itself by a local maximum in the region of minimum wall shear rate. It should be kept in mind that the limiting diffusion current is always positive no matter what the flow direction is.

Farther from the stagnation point at r/d = 2.50 and r/d = 3.01, the effect of vortices attenuates (see Fig. 11e and f). The coherent structures are far above the wall (see Fig. 5) and cause only sparse peaks on wall shear rate. There is no dominant frequency on the power spectra in Fig. 12e and f. Let us remember that the second local maxima of $\sqrt{\overline{\gamma'^2}}$, $\sqrt{\overline{Sh'^2}}$ and $\overline{Sh}$ distributions at r/d = 2.5 were explained by the presence of counter-rotating secondary vortices. From the analysis made above and based on the Fig. 13 extracted from [38] the presence of the counter-rotating secondary vortices are expected to be present in a wide region (r/d ~ 1.5 to 2.5). They are very close to the wall at r/d = 1.5 with a clear effect on the time evolution of wall shear rate γ(t) (see Figs 11d and 12d), and they are far above the wall at r/d= 2.5 where γ(t) is not more periodic. Even if these vortices are rather far from the wall, they induce a local maximum of the mean local Sherwood number and its fluctuations (Fig. 10a and b).

The histories of local mass transfer are shown in Fig. 14a and b, and the corresponding power spectral density are given in Fig.12. The thick concentration boundary layer on the platinum disc acts as a filter which attenuates high frequencies (Fig. 12). The second peak of γ_{cor} at 52.2 Hz is negligible on the spectra of *Sh* (Fig. 12c and d) and the impact of coherent structures results in the peak 26.1 Hz on the power spectra at $r/d < 1.5$. The fluctuations of *Sh* are caused by the normal velocity component. The largest fluctuations are at $r/d = 2.5$ (see Figs 10b and 14) due to large eddies. These eddies are random at a frequency about 1 Hz estimated from Fig. 14b.

Conclusions

The instantaneous values of local mass transfer and wall shear rate at an impinging wall were measured at the same points for the first time.

Numerous phenomena indicated by the measured quantities were analysed. A tomographic PIV measurements provided information on the organization of coherent flow structures, which play a role in the wall shear rate and the mass transfer phenomenon at the impinged wall.

The maximum of mean local Sherwood number was closer to the stagnation point ($r/d = 0.57$) than the maximum wall shear rate ($r/d = 0.69$). This difference was due to the dynamics of the Kelvin-Helmholtz (K-H) vortices approaching and impinging the wall. The turbulence created by the deflection of K-H vortices by the wall penetrated the laminar boundary layer and terminated the region of quasi-uniform accessibility to the mass transfer. As the mass transfer was increasing in this region, its termination corresponded to a maximum. The local maximum of the mean wall shear rate distribution corresponded to the point where the K-H vortices impinged the wall.

The peaks in the mean value and fluctuations of the local Sherwood number distributions which appeared approximately at $r/d = 2.5$ were related to the turbulence enhancement by the secondary counter-rotating vortices formed at the place where the K-H vortices detached from the wall.

The course of wall shear rate and local mass transfer close to their maxima ($r/d \sim 0.7$) was regular and periodical with sharp peaks and width valleys. This phenomenon was explained by the interaction of the primary K-H structures with smaller structures issued from the breaking-down of the primary K-H structures which rotate in the same direction. At this position, the

correction factor taking into account the inertia of the concentration boundary layer had a local minimum equal to 1.75.

The correction factor had its maximum (2.95) at *r/d*=1.47 where the course of instantaneous wall shear rate was periodic with large deformed peaks and sharp valleys. This phenomenon was related to the counter-rotating secondary vortices. They were present in a wide region (*r/d* ~ 1.5 to 2.5); around *r/d*= 1.5 their occurrence close to the wall resulted in a clear periodicity of the wall shear rate, whereas farther, at *r/d*= 2.5, the vortices moved apart the wall and the wall shear rate was not more periodic. The related free-stream turbulence affected the boundary layer at this position and generated local maxima in the mean value and fluctuations of Sherwood number.

The global Sherwood number obtained by integration of the local Sherwood numbers, under the hypothesis of axial symmetry, was 8.5% higher than the value obtained from the limiting diffusion current through the whole surface of the platinum disc. The Sherwood number calculated from the slope of the tangent to the radial distribution of wall shear rate in the stagnation region corresponded quite well to the global Sh in this region.

References

1. Webb, B.W. and C.F. Ma, *Single-Phase Liquid Jet Impingement Heat Transfer.* Advances in Heat Transfer, 1995. **26**: p. 105-217.
2. Jambunathan, K., et al., *A review of heat transfer data for single circular jet impingement.* International Journal of Heat and Fluid Flow, 1992. **13**: p. 106-115.
3. Kataoka, K. and T. Mizushina. *Local enhancement of the rate of heat-transfer in an impinging round jet by free-stream turbulence*. In *Heat Transfer 1974; Proceedings of the Fifth International Conference, Tokyo, Volume 2*. 1974. Tokyo.
4. Kataoka, K., et al., *Mass transfer between a plane surface and an impinging turbulent jet: the influence of surface-pressure fluctuations.* Journal of Fluid Mechanics, 1982. **119**: p. 91-105.
5. Alekseenko, S.V. and D.M. Markovich, *Electrodiffusion diagnostics of wall shear stresses in impinging jet.* Journal of Applied Electrochemistry, 1994. **24**: p. 626-631.
6. Phares, D.J., G.T. Smedley, and R.C. Flagan, *The wall shear stress produced by the normal impingement of a jet on a flat surface.* Journal of Fluid Mechanics, 2000. **418**: p. 351-375.
7. Chin, D.T. and M. Agarwal, *Mass transfer from an oblique impinging slot jet.* J. Electrochem. Soc., 1991. **138**(9): p. 2643-2650.
8. Alekseenko, S.V. and D.M. Markovich. *Local characteristics of impinging round jet*. In *3rd Int. Symp. on Engineering Turbulence Modelling and Measurements*. 1996. Crete, Greece.

9. Chin, D.T. and C.H. Tsang, *Mass Transfer to an Impinging Jet Electrode.* Journal of The Electrochemical Society, 1978. **125**(9): p. 1461-1470.
10. Kristiawan, M., et al., *Wall shear rates and mass transfer in impinging jets: Comparison of circular convergent and cross-shaped orifice nozzles.* International Journal of Heat and Mass Transfer, 2012. **55**: p. 282–293.
11. Meslem, A., et al., *Flow dynamics and mass transfer in impinging circular jet at low Reynolds number. Comparison of convergent and orifice nozzles.* International Journal of Heat and Mass Transfer, 2013. **67**(0): p. 25-45.
12. Lee, J. and S.J. Lee, *The effect of nozzle configuration on stagnation region heat transfer enhancement of axisymmetric jet impingement.* International Journal of Heat and Mass Transfer, 2000. **43**: p. 3497-3509.
13. Violato, D., et al., *Three-dimensional vortex dynamics and convective heat transfer in circular and chevron impinging jets.* International Journal of Heat and Fluid Flow, 2012. **37**: p. 22–36.
14. Roux, S., et al., *Experimental investigation of the flow and heat transfer of an impinging jet under acoustic excitation.* International Journal of Heat and Mass Transfer, 2011. **54**: p. 3277–3290.
15. Lytle, D. and B.W. Webb, *Air jet impingement heat transfer at low nozzle-plate spacings.* International Journal of Heat and Mass Transfer, 1994. **37**(12): p. 1687-1697.
16. Carlomagno, G.M. and A. Ianiro, *Thermo-fluid-dynamics of submerged jets impinging at short nozzle-to-plate distance: A review.* Experimental thermal and fluid science, 2014. **58**(0): p. 15-35.
17. Zuckerman, N. and N. Lior, *Jet Impingement Heat Transfer: Physics, Correlations, and Numerical Modeling.* Advances in Heat Transfer, 2006. **39**.
18. Hadziabdic, M. and K. Hanjalic, *Vortical structures and heat transfer in a round impinging jet.* Journal of Fluid Mechanics, 2008. **596**: p. 221-260.
19. Popiel, C.O. and O. Trass, *Visualization of a free and impinging round jet.* Experimental Thermal and Fluid Science, 1991. **4**: p. 253-264.
20. Gardon, R. and J.C. Akfirat, *Heat Transfer Characteristics of Impinging Two-Dimensional Air Jets.* Journal of Heat Transfer, 1966. **88**(1): p. 101-107.
21. El-Hassan, M., et al., *Experimental investigation of the wall shear stress and the vortex dynamics in a circular impinging jet.* Experiments in Fluids, 2012. **52**(6): p. 1475-1489.
22. Reiss, L.P. and T.J. Hanratty, *Measurement of instantaneous rates of mass transfer to a small sink on a wall.* AIChE Journal, 1962. **8**(2): p. 245–247.
23. Menendez, A.N. and B.R. Ramaprian, *The use of flush mounted hot film gauges to measure skin friction in unsteady boundary layers.* Journal of Fluid Mechanics, 1985. **161**: p. 139-159.
24. Sobolik, V., O. Wein, and J. Cermak, *Simultaneous measurement of film thickness and wall shear stress in wavy flow of new-Newtonian liquids.* Collection of Czechoslovak Chemical Communications, 1987. **52**(4): p. 913-928.
25. Sobolik, V., et al., *Calibration of electrodiffusion friction probes using a voltage-step transient.* Journal of Applied Electrochemistry, 1998. **28**(3): p. 329-335.
26. Hain, R., C. Kähler, and D. Michaelis, *Tomographic and time resolved PIV measurements on a finite cylinder mounted on a flat plate.* Experiments in Fluids, 2008. **45**(4): p. 715-724.
27. Wieneke, B., *Volume self-calibration for 3D particle image velocimetry.* Experiments in Fluids, 2008. **45**(4): p. 549-556.

28. Schmid, P.J., D. Violato, and F. Scarano, *Decomposition of time-resolved tomographic PIV.* Experiments in Fluids, 2012. **52**: p. 1567–1579.
29. Elsinga, G.E., et al., *Tomographic particle image velocimetry.* Experiments in Fluids, 2006. **41**(6): p. 933-947.
30. Atkinson, C., et al., *The accuracy of tomographic particle image velocimetry for measurements of a turbulent boundary layer.* Experiments in Fluids, 2011. **50**(4): p. 1031-1056.
31. Buchner, A.-J., et al., *Stereoscopic and tomographic PIV of a pitching plate.* Experiments in Fluids, 2012. **52**(2): p. 299-314.
32. Jeong, J. and F. Hussain, *On the identification of a vortex.* Journal of Fluid Mechanics, 1995. **285**: p. 69-94.
33. Gutmark, E.J. and C.M. Ho, *Preferred modes and the spreading rates of jets.* Physics of Fluids, 1983. **26**(10): p. 2932–2938.
34. Ball, C.G., H. Fellouah, and A. Pollard, *The flow field in turbulent round free jets.* Progress in Aerospace Sciences, 2012. **50**: p. 1–26.
35. Rajaratnam, N., *Turbulent jets*. 1976, Amsterdam, Netherlands: Elsevier Scientific Publishing Company.
36. Vallis, E.A., M.A. Patrick, and A.A. Wragg. *Techniques of wall measurements in fluid mechanics*. In *Euromech.90.* 1977. Nancy, France.
37. Colucci D, W. and R. Viskanta, *Effect of nozzle geometry on local convective heat transfer to a confined impinging air jet.* Experimental Thermal and Fluid Science, 1996. **13**(1): p. 71-80.
38. El Hassan, M., et al., *Experimental investigation of the wall shear stress in a circular impinging jet.* Physics of Fluids, 2013. **25**(7): p. 077101.
39. Reiss, L.P. and T.J. Hanratty, *An experimental study of the unsteady nature of the viscous sublayer.* AIChE Journal, 1963. **9**(2): p. 154-160.
40. Naguib, A.M. and M.M. Koochesfahani, *On wall-pressure sources associated with the unsteady separation in a vortex ring / wall interaction.* Physics of Fluids, 2004. **16**: p. 2613–2622.